Advances in Water Resources 149 (2021) 103855

Contents lists available at ScienceDirect

Advances in Water Resources

journal homepage: www.elsevier.com/locate/advwatres

Effects of topological disorder in unsaturated granular media via a pore-scale lattice Boltzmann investigation

Zhang Shi[a], Zhongzheng Wang[a,b], Yixiang Gan[a,*]

[a] School of Civil Engineering, The University of Sydney, Sydney, NSW 2006, Australia
[b] Navier, Ecole des Ponts, Univ Gustave Eiffel, CNRS, Marne-la-Vallée, France

ARTICLE INFO

Keywords:
Disordered porous medium
Retention curve
Relative permeability
Liquid cluster distribution
Shan-Chen lattice Boltzmann method

ABSTRACT

In this study, we investigate the impact of topological disorder on liquid distribution and transport phenomena in three-dimensional unsaturated granular media using the Shan-Chen lattice Boltzmann method. Distinct samples of disordered media are generated, characterized by the disorder index I_v. Under different I_v, varied liquid cluster distributions are demonstrated in a gravity-driven vapour-liquid system. Gradually increasing the initial liquid phase in the simulation domain allows the full range of saturation. The focuses are placed on the liquid cluster statistics from the connectivity, total cluster number, largest cluster and mean cluster volume at an increasing saturation. Meanwhile, the interfacial area, liquid retention curves and relative permeability-saturation curves are produced at diverse I_v and wettability. It is found that the slopes of retention curves are well correlated with the proposed capillary index I_c that unifies both disorder and wettability. The proposed generalized correlation between capillary index and slope index is useful in terms of determining the capillary pressure-saturation curve and relative permeability-saturation curve for a given granular system at varied contact angles. Additionally, the cohesive strength-saturation curves are also obtained with the aid of the interfacial area and negative capillary pressure, which elucidates that a packing with a higher I_v experiences a relatively larger cohesive strength. These results enhance the understanding of disorder effect and will be beneficial for the exploration of many retention curves-related phenomena such as liquid transfer and stress-strain relation for wet granular media.

1. Introduction

Granular materials in nature or industry usually consist of three phases, including air, liquid, and solid grains. The interaction among them is critical in determining both hydraulic and mechanical properties of partially saturated granular media (Fournier et al., 2005; Sheng, 2011). For example, the rainfall-induced slope instability is caused by the decrease of shear strength under an increasing water saturation in soil (Zhu and Anderson, 1998). In the field of unsaturated porous media, the water retention curve (WRC) is a fundamental correlation, which introduces the variation of capillary pressure with the water saturation (Brooks and Corey, 1964; van Genuchten, 1980). The accurate representation of this curve is of importance in many practical aspects, such as the determination of shear strength and water relative permeability (Zhou et al., 2016; Sheng et al., 2019). That is, the capillary pressure-saturation equation can be embedded in the analytical expression of shear strength or relative permeability. Thus, an increasing focus is put on investigating the WRC and its dependence (Ahrenholz et al., 2008; Zhou, 2013; Likos et al., 2014). The WRC as a macroscopic feature is a result of the pore-scale liquid distribution at varied saturation, governed by the surface and geometrical characteristics in porous media, including the surface tension, contact angle and pore-size distribution, which have been already explored in many studies (Zhou, 2013; Likos and Jaafar, 2013; Delenne et al., 2015; Wang et al., 2017). As many natural porous media are heterogeneous with varied pore characteristics, the effects of topological disorder of porous media on the two-phase fluid displacement has attracted an increasing attention (Holtzman and Juanes, 2010; Holtzman, 2016; Hu et al., 2019; Lu et al., 2019). However, less studies have been conducted on the impact of topological disorder on unsaturated porous media with focusing on the liquid cluster distribution, interfacial area, capillary pressure and relative permeability.

The liquid distribution under the capillary condensation process has been modelled with the identification of four states including pendular, early funicular, late funicular and capillary states, which shows a strong correlation with the WRC (Delenne et al., 2015). Zhou (2013) developed a contact angle hysteresis-dependent model for the water retention curve, which shows the difference of WRC between the drainage and imbibition process. Li et al. (2018) analyzed the effects of heterogeneity, grain surface area, contact angle and surface tension on the

* Corresponding author.
E-mail address: Yixiang.Gan@sydney.edu.au (Y. Gan).

https://doi.org/10.1016/j.advwatres.2021.103855
Received 12 October 2020; Received in revised form 16 January 2021; Accepted 16 January 2021
Available online 20 January 2021

interfacial area, capillary pressure and relative permeability in a steady-state two-phase flow. The computed interfacial area is also used to describe the fluid distribution, and the heterogeneous medium is found to experience a larger capillary pressure, smaller relative permeability and fluid-fluid interfacial length at a given saturation, compared with a relatively uniform medium. For the fluid displacement, Bakhshian and Hosseini (2019) studied the impact of wettability heterogeneity on the CO_2-brine displacement in rock samples of Tuscaloosa sandstone, finding that an increasing percentage of CO_2-wet regions during drainage leads to a more stable displacement, a lower CO_2 relative permeability and capillary pressure at a given brine saturation. Bakhshian et al. (2020) probed the interaction between wettability and pore geometry on the fluid displacement by adopting homogeneous and heterogeneous porous media at varied wettability. In addition to above factors, the disorder of porous media modifies the mode of two-phase flow through varying the shape of pore and throat size distributions (Wang et al., 2019; Lu et al., 2019). A highly disordered porous medium is preferred to enhance the liquid retention behaviour in a gravity-driven drainage, through providing a wide trapped saturated cluster distribution (Cui et al., 2019). The interplay between the wettability and the degree of disorder on the fluid displacement has been explored by Wang et al. (2019), by proposing a correlation between the interfacial length and invading saturation with the incorporation of both disorder and wettability. Nevertheless, as with the aforementioned studies, the direct correlation between the disorder and liquid distribution in partially saturated porous media has not been developed.

Analytical, experimental and numerical approaches have been adopted to study the behaviour of unsaturated porous media. Pore-scale water retention hysteresis models have been developed based on the representation of void space by classical cylindrical capillaries (Likos and Jaafar, 2013; Ferraro et al., 2017). However, the capillary properties are often obtained according to the statistical distribution and cannot capture the information at pore scale. The hysteresis of WRCs can also be computed via the drainage and imbibition experiments under a glass bead packing, and the fluid interfacial area can be obtained through using X-ray microtomography to reveal the unsaturated flow (Culligan et al., 2004; Porter et al., 2010). In addition, the existing numerical models include the pore-network model (Joekar-Niasar et al., 2010), volume of fluid (Cui et al., 2019), and lattice Boltzmann methods (Schaap et al., 2007; Li et al., 2018; Nekoeian et al., 2018). Although the pore-network model is advantageous in terms of the computation efficiency, it is limited to the simplified pore information and flow equations (Joekar-Niasar et al., 2010; Tranter et al., 2018). The volume of fluid method is also proposed to study the unsaturated flow (Cui et al., 2019), but this method is computationally expensive, which limits its applicability for simulating larger-scale three-dimensional unsaturated flow. Alternatively, the lattice Boltzmann method (LBM) is another powerful tool to reveal pore-scale unsaturated flow in porous media, which is employed by many recent investigations due to its superiority of handling the complex geometry, readily capturing the interface and vastly parallel computation (Yang and Boek, 2013; Chen et al., 2014; Li et al., 2018; Nekoeian et al., 2018; Bakhshian et al., 2019). Among many multiphase models in the LBM, Shan-Chen single-component model is proved to be competent in simulating the liquid-gas flow with a high density ratio (Sukop and Or, 2004; Huang and Lu, 2009; Chen et al., 2014). The study carried by Sukop and Or (2004) is based on the singe-component model, showing numerical liquid retention curves in silts and in angular pores, validated by the theoretical equations. The similar model was adopted by Huang and Lu (2009) to study the gas-liquid distribution, which has been validated by comparing the numerical velocity profile and relative permeability in a two-dimensional channel with analytical solutions.

This paper presents a pore-scale investigation using the lattice Boltzmann method to study gravity-driven unsaturated flow in three-dimensional disordered porous media with varied surface wettability. Distinct porous samples containing spherical grains are generated with the introduction of the disorder index I_v, which characterizes the degree of topological disorder. By gradually increasing the initial saturation of liquid phase in the simulation domain, different states are achieved from a pendular to a fully saturated state. The effects of disorder on the distribution of liquid cluster as well as the interfacial area are analysed at different saturation. The capillary pressure-saturation and relative permeability-saturation curves are then demonstrated under varied disorder and wettability, with constructing the relation between the slope index and the capillary index I_c that unifies both disorder and wettability effects. The obtained relation can be used to predict the overall shape of these two critical curves. The cohesive strength induced by the negative capillary pressure is further discussed under varied I_v and wettability.

2. Method

2.1. Generation of disordered media

The porous medium is a rectangular cuboid filled with mono-sized spherical obstacles initially hexagonal close-packed (HCP) as the solid phase. Then, the Monte-Carlo iterative movement is applied to each obstacle to introduce topological disorder, with considering the periodic boundary condition in all directions. The Voronoi method is used to tessellate the pore space for the analysis of disorder. The disorder index I_v is given as the fluctuation of the local porosity, ϕ_i, calculated from each Voronoi cell as (Cui et al., 2019):

$$I_v = \{\langle \phi_i^2 \rangle - \langle \phi_i \rangle^2\}^{1/2} \tag{1}$$

where the operator $\langle \cdot \rangle$ corresponds to the volume average. Compared to the traditional disorder index based on regular meshes (Laubie et al., 2017), the used disorder index can capture the small variation in microstructures (Cui et al., 2019). This index can be another way of expressing the pore size distribution. But it provides more information about the throat size distribution. Importantly, it is simple to use one single parameter (i.e., the disorder index) to characterise the effects of polydispersity of granular media. During the Monte-Carlo moves, the degree of disorder is controlled by the apparent diameter $D_{app} = \lambda D$ with $\lambda \in [1, D_{max}/D]$ where D and D_{max} are the particle diameter and the diameter for the closed packing, respectively (Laubie et al., 2017; Wang et al., 2019). Therefore, $\lambda = 1$ represents the system with the maximum I_v where the spheres are free to move without overlap, while $\lambda = D_{max}/D$ represents the hexagonal packing. Under a given λ, sufficient steps are run to obtain the stabilized I_v. It is noted that the maximum I_v depends on the size, packing factor and number of spheres of porous medium. Although current work only involves the monodisperse packing, the above method can be extended to consider the polydisperse packing (Zakirov and Khramchenkov, 2020).

Using the above generation method of disordered packing, four distinct porous media consisting of 128 solid grains are generated with the disorder index $I_v = 0.013, 0.030, 0.050$ and 0.073 shown in Fig. 1(a). The radius of spherical obstacle is 20 lattice unit with the maximum apparent radius of 22 lattice unit, which makes the overall packing factor of 0.556. To achieve statistical information of pores and throats, Delaunay tessellation is then conducted for the pore space tessellation. The volume of each pore is equal to the volume of corresponding Delanuay tetrahedron without the solid section, shown in Fig. 1(c). The throat size is calculated as the maximal inscribed radius of triangular face in Delanuay tetrahedrons, as in Fig. 1(d). With an increasing I_v, the packing tends to become more disordered, which is reflected by the pore volume and throat size distribution as shown in Fig. 1(c) and 1(d), respectively. It is seen that a larger disorder index leads to a wider distribution for both pore volume and throat size. Note that, for a better visible comparison, the maximum pore volume is not displaced at the tail of the probability distribution in Fig. 1(c).

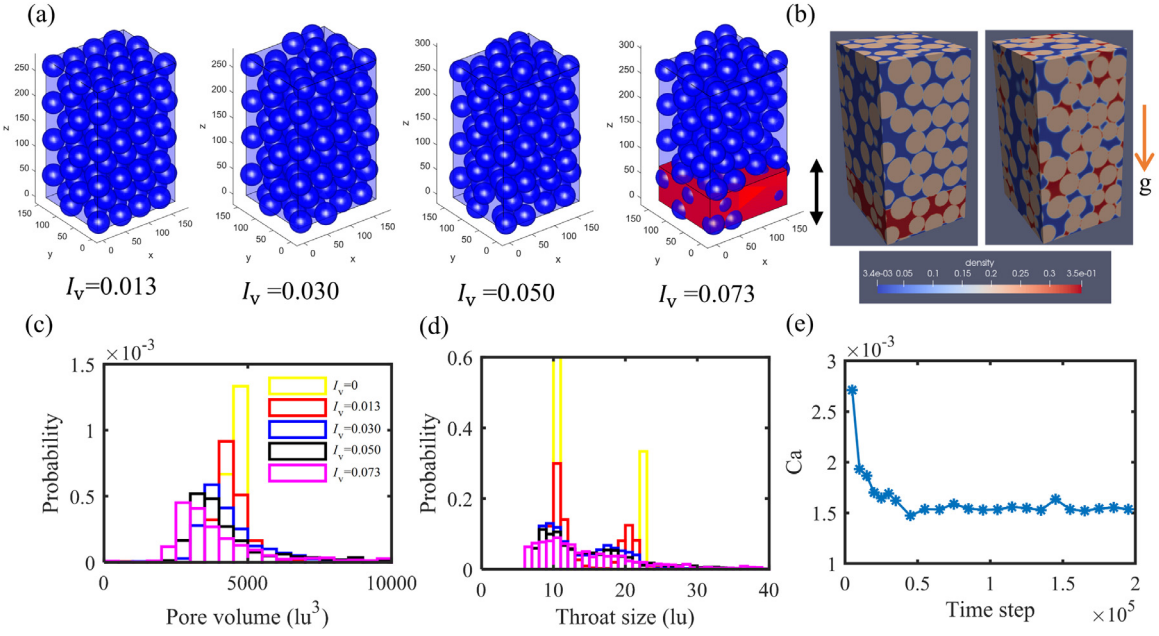

Fig. 1. (a) Generated porous media with the packing factor of 0.556 and $I_v = 0.013, 0.030, 0.050, 0.073$ from left to right. (b) The initial configuration (left) and final liquid distribution (right) under the gravity g in the LBM. The red, blue and brown colors represent the liquid, vapour and solid grains, respectively. The height of liquid phase is adjusted to reflect varied saturation. (c) The pore volume and (d) throat size distributions with an increasing I_v. (e) Typical evolution of capillary number as a function of time step.

2.2. Simulation method

To numerically study two-phase flow into disordered porous media, we implement the Shan-Chen single-component multiphase lattice Boltzmann method in three dimensions with the use of D3Q19 lattice (Shan and Chen, 1994). The density distribution function under the Bhatnagar-Gross-Krook (BGK) collision operator satisfies the following lattice Boltzmann equation (Bhatnagar et al., 1954):

$$f_i(x + c_i\Delta t, t + \Delta t) = f_i(x,t) - \frac{\Delta t}{\tau}(f_i(x,t) - f_i^{eq}(x,t)) \tag{2}$$

where f_i is the density distribution in ith velocity direction, and τ is a relaxation time, leading to the kinematic viscosity as $\nu = c_s^2(\tau - 0.5\Delta t)$ in lattice unit, where c_s denotes of the speed of sound. Although the multiple-relaxation-time (MRT) model can improve the uncertainty when the relaxation time is close to 0.5, it is demonstrated that both BGK and MRT models can yield similar results at the relaxation time of 1 (Pan et al., 2006). Therefore, the relaxation time in our study is set up to be 1.0 so that the applied BGK model is feasible with the ranges of relevant model parameters and preferred due to less computation complexity. The equilibrium distribution function f_i^{eq} is calculated by

$$f_i^{eq}(x,t) = \omega_i\rho\{1 + \frac{u\cdot c_i}{c_s^2} + \frac{(u\cdot c_i)^2}{2c_s^4} - \frac{u\cdot u}{2c_s^2}\} \tag{3}$$

where ω_i denotes the weighting factor in the ith direction, u denotes the macroscopic equilibrium fluid velocity and ρ denotes the fluid density. In current case, D3Q19 is adopted as a velocity set to solve the Navier-Stokes equations in three dimensions. Therefore, c_i is given by

$$c_i = c_u \begin{bmatrix} 0 & 1 & -1 & 0 & 0 & 0 & 0 & 1 & -1 & 1 & -1 & 0 & 0 & 1 & -1 & 1 & -1 & 0 & 0 \\ 0 & 0 & 0 & 1 & -1 & 0 & 0 & 1 & -1 & 0 & 0 & 1 & -1 & -1 & 1 & 0 & 0 & 1 & -1 \\ 0 & 0 & 0 & 0 & 0 & 1 & -1 & 0 & 0 & 1 & -1 & 1 & -1 & 0 & 0 & -1 & 1 & -1 & 1 \end{bmatrix} \tag{4}$$

where $c_u = \Delta x/\Delta t$ represents the lattice speed, and Δx is the lattice spacing. In Eq. (3), for the D3Q19 model, $\omega_i = \frac{1}{3}$ for $i = 0$; $\omega_i = \frac{1}{18}$ for $i = 1, 2, 3 \cdots 6$; $\omega_i = \frac{1}{36}$ for $i = 7, 8, 9 \cdots 18$. The density of the fluid in Eq. (3) is given as $\rho = \sum f_i$, and the macroscopic velocity can be then computed as

$$u = u' + \frac{\tau F}{\rho} \tag{5}$$

where $u' = \frac{\sum f_i c_i}{\rho}$, and F denotes the total force acting on the lattice site. The total force includes the interaction force (F^{sc}) due to the surface tension, the adhesion force (F^{ad}) due to the wettability and the external force, F^b (i.e., gravity in this study), as $F = F^{sc} + F^{ad} + F^b$.

The Shan-Chen single-component multiphase model introduces an interaction force as (Shan and Chen, 1994)

$$F^{SC}(x) = -G\psi(x)\sum_i \omega_i\psi(x + c_i\Delta t)c_i\Delta t \tag{6}$$

where ψ is the pseudopotential function, or the effective mass, depending on the local density, and G is the strength parameters that can characterize the interaction between different phases. To achieve the phase separation, G should be negative, which represents the attractive force between lattice nodes. This expression can also account for the fluid-solid interaction (i.e., wettability) by tuning the wall density so that the variation of contact angles can be controlled (Benzi et al., 2006). From the equation of state of Shan-Chen model, the pressure at any node is given as

$$p = c_s^2\rho + \frac{c_s^2 G}{2}\psi^2(\rho). \tag{7}$$

Re-arranging Eq. (7) obtains

$$\psi(\rho) = \sqrt{\frac{2(p - c_s^2\rho)}{c_s^2 G}}. \tag{8}$$

To minimize the spurious velocity, the Carnahan-Starling equation of state is applied in Eq. (8) as (Yuan and Schaefer, 2006)

$$p = \rho RT\frac{1 + b\rho/4 + (b\rho/4)^2 - (b\rho/4)^3}{(1 - b\rho/4)^3} - a\rho^2 \tag{9}$$

with $a = 0.4963R^2T_c^2/P_c$, $b = 0.18727RT_c/P_c$, and R and T are the gas constant and temperature, respectively. From the above equations, the critical temperature, T_c can be calculated. The phase separation does

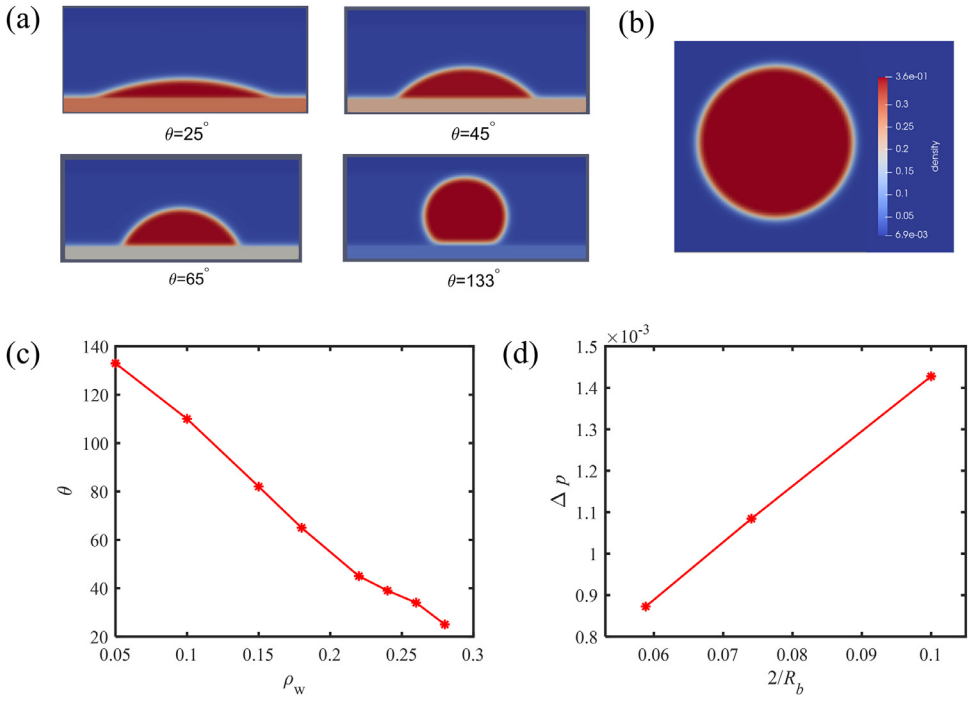

Fig. 2. (a) The benchmark of contact angles when different wall densities are set up. (b) The sample of bubble test. (c) Contact angle θ as a function of fictitious wall density ρ_w. (d) The pressure drop Δp across the interface for different bubble radii R_b. The surface tension can then be computed through the Young Laplace equation as $\Delta p = 2\gamma / R_b$.

not occur if $T > T_c$. Note that the value of G does not influence the simulation results as it is cancelled out with the substitution of Eq. (8) into Eq. (6). The density ratio and surface tension are determined by the input temperature. A lower temperature leads to a higher density ratio and surface tension. Given the fact that the Shan-Chen two-component model shows the incompetency when the viscosity ratio is over 5 (Yang and Boek, 2013), the adopted single-component model is an ideal selection for the liquid-vapour system and is proven to be capable to simulate high density ratio fluids (Sukop and Or, 2004; Huang and Lu, 2009; Chen et al., 2014).

The generated packing with varied I_v are imported into the lattice Boltzmann modelling with the total lattice number of $M \times N \times Z = 152 \times 176 \times 287$. The radius of sphere R_s is set to be 20 lattice unit (lu) for the convergence purpose (Pan et al., 2004). We set $a = 1$, $b = 4$, $R = 1$ and $T = 0.7T_c$ in the equation of the state shown in Eq. (9), which yields an equilibrium density of vapour and liquid with 0.005 and 0.352 in the lattice unit system, respectively. The density ratio is calculated as 70. The current temperature is chosen for the numerical stability and this input temperature has been also adopted in other studies (Richefeu et al., 2016; Huang and Lu, 2009). Initially the liquid occupies the region near the bottom, while the rest of pore space is occupied by the vapour phase as in Fig. 1(b). Periodic boundary conditions are applied in all directions to avoid the boundary effect, i.e., outflowing liquid or vapour re-enters the domain through the opposite boundary. The height of wetting phase can be modified to vary the saturation in the whole domain. With the relaxation time $\tau = 1$, the value of kinematic viscosity is calculated to be 0.167 for both phases, resulting in the kinematic viscosity ratio of 1. The density difference between liquid and vapour causes the dynamic viscosity ratio of 70. The magnitude of liquid-vapour surface tension γ is determined as 0.015 through the bubble test. The variation of contact angles between liquid phase and grain surface is achieved by altering the fictitious wall density. The benchmark of surface tension and contact angle is summarised in Fig. 2. The gravity g with a value of 0.00032 is applied vertically downwards, corresponding to a bond number of $Bo = \Delta\rho g {R_s}^2 / \gamma \cdot e = 3.68$, where e denotes the void ratio (Cui et al., 2019). Although a larger surface tension is always preferred for considering the capillary effect, the bond number in this case can demonstrate both gravitational and capillary effects. The calculated Reynolds number is less than 10. For the conversion of lattice units towards physical values, three reference quantities including length scale l_0, time scale t_0 and mass scale m_0 are applied as $l_0 = 8 \times 10^{-6}$ m, $t_0 = 7.2 \times 10^{-7}$ s and $m_0 = 1.46 \times 10^{-12}$ kg. Consequently, the physical particle radius becomes $R_s \times l_0 = 1.6 \times 10^{-4}$ m, the physical liquid density and dynamic viscosity are obtained as $\rho_{\text{phy}} = \rho m_0 / {l_0}^3 = 1000\ \text{kg} \cdot \text{m}^{-3}$ and $\mu_{\text{phy}} = \nu\rho \frac{m_0}{l_0 t_0} = 2.49 \times 10^{-3}$ Pa · s, respectively. The physical liquid-vapour surface tension and gravity are computed as $\gamma_{\text{phy}} = \gamma m_0 / {t_0}^2 = 42.2\ \text{mN} \cdot \text{m}^{-1}$ and $g_{\text{phy}} = g l_0 / {t_0}^2 = 4.94 \times 10^3\ \text{m} \cdot \text{s}^{-2}$, respectively. Table 1 summarises geometrical parameters of studied porous media and properties of two phases in both lattice and physical unit systems.

The simulations are initialized with a zero velocity field, and then runs 2.0×10^5 time steps, which is found to be sufficient to reach the equilibrium state, see Fig. 1(e) for a typical evolution. Overall, 10 saturation values from 0 to 1 are simulated with different disorder indexes ($I_v = 0.013, 0.030, 0.050, 0.073$) and contact angles ($\theta = 25°, 45°, 82°, 133°$). Note that the case with $I_v = 0.073$ and $\theta = 25°$ is not carried out due to the numerical instability reason, i.e., in total 150 cases. The multiple-relaxation-time method instead of BGK method can be adopted in the future to deal with the instability problem. All simulations are run using The University of Sydney's High Performance Computing (HPC).

2.3. Data processing

Upon the simulation completion, the LBM exports data consisting of density and velocity of each lattice node with respect to the time step. The post-processing procedure includes the conversions from the raw data to preferred variable, e.g., saturation, capillary pressure, interfacial area, liquid cluster distribution and relative permeability. Before the conversions, the lattice nodes need to be identified as either the vapour, liquid, interface or solid phase based on empirical threshold densities. In this study, the lattice nodes with density greater than 0.26 lu are regarded as the liquid, the number of which is calculated as N_l. While if the density of the lattice nodes are smaller than 0.09 lu, the nodes are regarded as the vapour, the number of which is calculated as N_v. The nodes with density between these two threshold values is considered as the liquid-vapour interface node with the number of N_i. The solid

Table 1
Geometrical parameters of disordered porous media and properties of two phases.

Parameters	Lattice unit		Physical unit	
Domain size	$152 \times 176 \times 287$	l_0^3	$1.22 \times 1.41 \times 2.30$	mm^3
Radius of particle	20	l_0	0.16	mm
Liquid density	0.352	$m_0 \cdot l_0^{-3}$	1000	$kg \cdot m^{-3}$
Liquid dynamic viscosity	5.87×10^{-2}	$m_0 \cdot l_0^{-1} t_0^{-1}$	2.49×10^{-3}	$Pa \cdot s$
Vapour density	0.005	$m_0 \cdot l_0^{-3}$	14.3	$kg \cdot m^{-3}$
Vapour dynamic viscosity	8.35×10^{-4}	$m_0 \cdot l_0^{-1} t_0^{-1}$	3.53×10^{-5}	$Pa \cdot s$
Gravity	3.2×10^{-4}	$l_0 \cdot t_0^{-2}$	4.94×10^{3}	$m \cdot s^{-2}$
Liquid-vapour surface tension	0.015	$m_0 \cdot t_0^{-2}$	42.2	$mN \cdot m^{-1}$

nodes with the number of N_s are located when the density equals the wall density that depends on the input of contact angles. A sensitivity analysis of the threshold values has been conducted and it is found that variations near the selected thresholds do not significantly affect the results.

The liquid retention curve is critical in two-phase flow, which describes the relationship between the liquid saturation and capillary pressure. The liquid saturation S is defined as

$$S = \frac{N_l + 0.5N_i}{M \times N \times Z - N_s}. \tag{10}$$

On average at varied saturation, the liquid-vapour interface nodes account for 5% of the total nodes. Although there are only few interface nodes, they are still counted in the saturation calculation and distributed equally for the liquid and vapour saturation (Li et al., 2018). However, these interface nodes induce the unfavourable spurious velocity and are excluded in the calculation for the flow rate (Connington and Lee, 2012). The capillary pressure P_c, defined as the difference between average vapour pressure U_v and liquid pressure U_l, is given as $P_c = U_v - U_l$, and the pressures are direct functions of densities according to the equation of state as in Eq. (9) (Delenne et al., 2015; Richefeu et al., 2016; Li et al., 2018; Nekoeian et al., 2018). The interfacial area is also needed in this study to analyze the fluid distribution and cohesive strength. Once the liquid phase is identified, the *isosurface* function in MATLAB can be used to generate the surface area of liquid, A_l, which is then normalised by the total volume of the domain (Porter et al., 2010). The surface area of vapour, A_v, and solid phase, A_s, are obtained using the same method. Subsequently, the liquid-vapour area, A_{vl}, the liquid-solid area, A_{ls} and vapour-solid area, A_{vs} are computed as (Culligan et al., 2004; Porter et al., 2010)

$$A_{lv} = \frac{A_l + A_v - A_s}{2},\ A_{ls} = A_l - A_{vl},\ A_{vs} = A_v - A_{vl}. \tag{11}$$

In the meantime, with the location of the liquid nodes, using *bwconncomp* function in a Matlab environment can help to determine the connected components. The post-processing includes relabeling components at the domain edges to comply with the periodic boundary condition, which allows to obtain the distribution of liquid cluster.

As stated above, the interface nodes are excluded in the calculation of the flow rate due to the spurious velocity. As the gravity is only applied vertically and volume-average fluxes in x and y directions are nearly zero, only velocities in z-direction are taken into account and the corresponding volume-averaging fluxes of liquid q_l and vapour q_v are given by

$$q_l = \frac{1}{M \times N \times Z} \sum^{N_l} U_{zl},\ q_v = \frac{1}{M \times N \times Z} \sum^{N_v} U_{zv}, \tag{12}$$

where U_{zl} and U_{zv} are the velocity of each lattice node in z-direction for the liquid and vapour, respectively. Then, the relative permeability of liquid k_{rl} and vapour k_{rv} are defined as (Li et al., 2018)

$$k_{rl} = \frac{q_l \nu}{k_i g},\ k_{rv} = \frac{q_v \nu}{k_i g} \tag{13}$$

where k_i is the intrinsic permeability, measured using single-phase flow into disordered media with $k_i/{R_s}^2$ of 5.62×10^{-3}, 7.01×10^{-3}, 9.49×10^{-3} and 1.36×10^{-2} for $I_v = 0.013,\ 0.030,\ 0.050,\ 0.073$, respectively (see Appendix for details); ν represents the kinematic viscosity of each phase. The capillary number can be considered an indicator of the equilibrium state, which is computed as $Ca = q_l \mu_l / \gamma$ where μ_l represents the dynamic viscosity of liquid and γ represents the surface tension. The capillary number is observed to keep nearly unchanged after 2.0×10^5 simulation time steps as shown in Fig. 1(e).

3. Results and discussion

3.1. Cluster statistics

We aim to find the disorder effect on the liquid clusters under the fixed wettability of 45°. When the solid surface has a lower wettability (i.e., at the contact angle of 82° and 133°), the number of identified liquid clusters in current domain is less than 10, which is not enough for the cluster statistical analysis. However, the number of liquid clusters increases with a decreasing contact angle, and therefore we choose the contact angle of 45° as a typical example. The cases under an even smaller contact angle (i.e., 25°) follow the same trend as those under 45°. In the following sections for the analyse of interfacial area, capillary pressure and relative permeability, the wettability effect will be considered. The pore-scale phenomena of liquid cluster distribution are critical in determining the macroscopic behaviour of wet granular packing, e.g., capillary pressure and relative permeability. Fig. 3(a) displays four typical snapshots of liquid cluster distribution with an increasing liquid saturation for $I_v = 0.030$, showing the pendular, funicular and capillary states. The pendular state is where the wetting phase exists in the form of liquid bridges between a pair of grains, and the saturation is low (less than 0.1). In the funicular state, the wetting phase binds more than 2 grains. The capillary state refers to the condition that grains are fully immersed in the wetting phase with only isolated nonwetting phase. In Fig. 3(a), for $S = 0.014$, all liquid exists in the form of liquid bridges, which shows the pendular state. In this state, each liquid cluster only connects two solid grains. At an increasing saturation, the funicular state is recognized via observing the coalescence of some liquid bridges when $S = 0.176, 0.275$, and a number of liquid clusters connect more than two solid grains. A percolating cluster is apparently observed for $S = 0.275$ and we also define this state as the funicular because it has one or more main percolating liquid cluster and a number of isolated liquid clusters. With a further increase in saturation, all solid grains are immersed in liquid at $S = 0.797$. This is defined as the capillary state where only one liquid cluster exists and it connects all 128 solid grains in the current system. These different snapshots show the cluster evolution and the feasibility of current simulation setup.

To more quantitatively compare the liquid distribution at different saturation, the cluster connectivity C is defined as the number of solid grains connected by a single cluster, which is then normalised by the total number of grains in the system (i.e., 128). The connectivity of each cluster is averaged to obtain the normalised mean connectivity of the system, C_n. Fig. 3(b) shows the mean connectivity of varied disordered media with saturation S. The mean liquid connectivity increases with saturation from 0.15625 ($\frac{2}{128}$) to 1 ($\frac{128}{128}$), because each liquid cluster

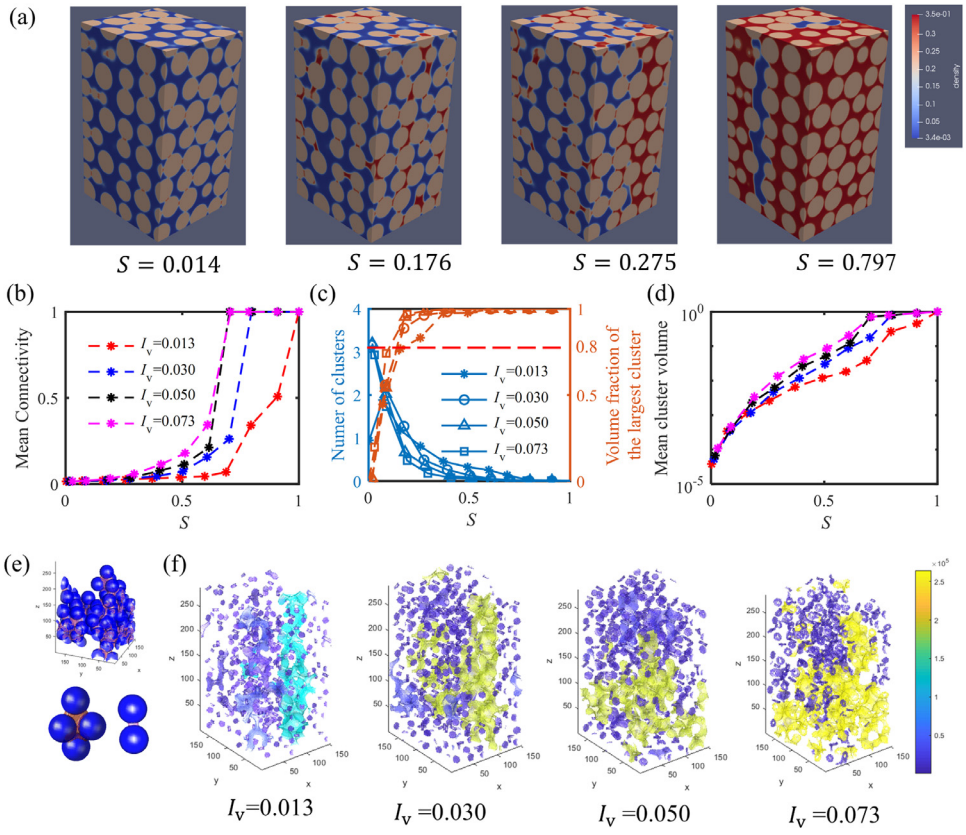

Fig. 3. (a) Snapshots of liquid distribution with increasing saturation from left to right for $I_v = 0.030$. The red, blue and brown colors represent the liquid, vapour and solid grains, respectively. (b) The normalised mean liquid connectivity as a function of saturation at different I_v with examples of cluster connectivity shown in (e). (c) The normalised number of clusters and the volume fraction of the largest cluster volume as a function of saturation, with the proposed red dash line as a guide to separate the funicular state from the pendular state. (d) The normalised mean cluster volume as a function of saturation. (e) Examples of cluster morphologies. (f) Liquid cluster morphologies under varied disordered media at $S = 0.08$. The color map represents the volume of cluster in lattice unit. (For interpretation of the references to color in this figure legend, the reader is referred to the web version of this article.)

starts from a liquid bridge with a connectivity of $\frac{2}{128}$, and in the end, a single cluster is formed and connects all of 128 grains. It is observed that a porous medium with a larger I_v has a larger mean liquid connectivity at a given saturation. This explains the phenomenon observed by Cui et al. (2019) that disorder facilitates the merging of clusters, thus connecting more grains (Cui et al., 2019), i.e., there are more dense packing zones in medium with a high degree of disorder. As a result, large saturated zones occur more frequently in a more disordered packing and it is more likely for these zones to join together to form a percolating cluster. To summarize, the disorder can enhance the cluster connectivity and the formation of percolating clusters.

As the total cluster number and volume change with the connectivity, the focus is then put on the influence of disorder on them. Fig. 3(f) depicts the cluster volume distribution of varied disordered packing at the saturation of 0.08, showing that a packing with a larger I_v has the largest percolating cluster. The volume of the largest cluster is then normalised by the current total cluster volume, and the number of liquid clusters is normalised by the total number of grains. Fig. 3(c) shows the normalised number of liquid clusters and the normalised volume of the largest liquid cluster as a function of saturation. The number of clusters is found to decreases with an increasing saturation due to the coalescence of adjacent clusters. Under the same saturation, a higher degree of disorder causes a smaller cluster number. The reason for this phenomenon is explained in the discussion of cluster connectivity that the disorder promotes the cluster coalescence to reduce the total cluster number. After the saturation of 0.8, there is no significant difference among varied disordered packing on the cluster number. Regarding the normalised volume of the largest cluster, it can be seen that the normalised volume for a higher disordered packing approaches one early. Here we define the threshold of normalised volume with 0.8 to distinguish the pendular from the funicular state based on the observed transition at $S \approx 0.2$ in the second subfigure of Fig. 4(b). Beyond that value, a single cluster can account for most of the liquid phase and less isolated clusters occur in the domain. We consider this state as a funicular state. Less than the threshold value, most of clusters exist in an isolated form, which is considered as a pendular state. It is revealed that the disorder can make wet porous media enter the funicular state early, with the increase of saturation. It is noted that a threshold of 0.8, used in current study, is only chosen for the comparison reason to obtain the qualitative conclusion of disorder effect on different states. More discrete saturation points near the transition region need to be simulated for further quantitative investigation. The relation between the normalised mean cluster volume and saturation is further demonstrated in Fig. 3(d). It is not surprising that an increase in the disorder index leads to an increasing mean cluster volume at the same saturation. This is because the disorder causes a less total number of clusters as depicted in Fig. 3(c).

3.2. Effect of wettability

After the investigation of pore-scale cluster distribution, the attention is then put on the effect of packing disorder on the interfacial area as well as the macroscopic behaviour including capillary pressure and relative permeability. Varied liquid contact angles are applied including $\theta = 25°, 45°, 82°, 133°$ to demonstrate the combined impacts of topological disorder and wettability.

3.2.1. Interfacial area

The enhancement of cluster merging induced by the disorder can be reflected from the interfacial area including A_{ls} and A_{vs} and A_{lv}. Fig. 4 demonstrates the variation of three types of interfacial area, normalised by the total volume of the domain, as a function of saturation for varied I_v at different contact angles ($\theta = 25°, 45°, 82°, 133°$). For $\theta < 90°$, it can be seen that a higher degree of disorder results in a larger liquid-solid interfacial area. It is because that the disorder causes a larger mean liquid cluster connectivity at the same saturation. The liquid cluster in the disordered media tends to attach more solid surface. In the meantime, less vapour-solid interfacial area is observed with

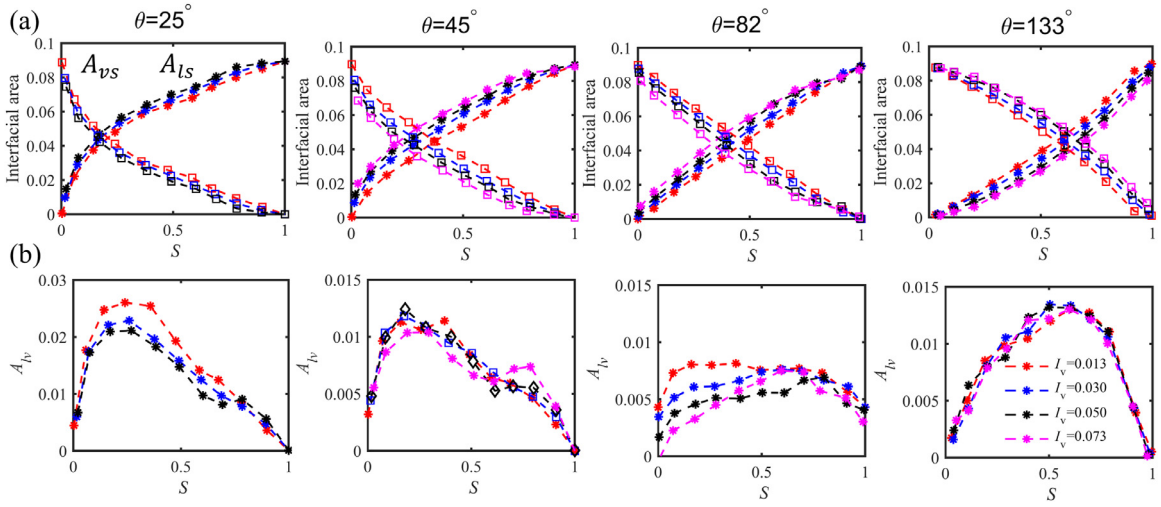

Fig. 4. (a) The normalised liquid-solid A_{ls} and vapour-solid interfacial area A_{vs} as a function of saturation. (b) The normalised liquid-vapour interfacial area as a function of saturation.

an increasing I_v. Similar tendencies are also identified in the work by Li et al. (2018) who made a comparison of interfacial area among varied heterogeneous porous media. However, when $\theta > 133°$, the reverse trend is identified that an increasing I_v leads to a decrease in A_{ls} and an increase in A_{vs} due to the hydrophobic grain surface. The liquid-solid interfacial area is a key parameter affecting the relative permeability. The increase in A_{ls} leads to a significant decrease in the liquid relative permeability, shown in Fig. 8. The disorder results in a larger liquid-solid interfacial area while leads to a decrease of relative permeability. The disorder effect on the relative permeability will be discussed further in the following Section. Besides, for the wettability effect, A_{ls} for the same I_v becomes larger at a smaller θ because the liquid clusters are more discrete in terms of distribution at the strong wettability. For the weak wettability, the liquid clusters become connected, and less isolated clusters are formed. Another observation from Fig. 4(a) is that the curve for the liquid-solid interfacial area is sharper for the strong wettability ($\theta = 25°$), while becomes straight line for the neutral wettability ($\theta = 82°$). With the increase of contact angle, the intersection saturation between the liquid-solid and vapour-solid interfacial area increases. For the nearly neutral wettability (i.e., $\theta = 82°$), the intersection occurs close to $S = 0.5$. That is, both liquid and vapour attach nearly the same area of solid surface at the equivalent saturation.

Regarding the liquid-vapour interfacial area shown in Fig. 4(b), a peak value is found at $S \approx 0.2$, followed by a drop when $\theta = 25°$ or 45°. This trend is also shown in the drainage and imbibition experiments conducted by Culligan et al. (2004). That peak point can correspond to the transition from the pendular to funicular state. When $\theta = 82°$ or 133°, a peak value can also be observed and it occurs at $S > 0.5$. Therefore, an increase in wettability makes the peak value of A_{lv} occur at a smaller S. Additionally, the disorder effect on A_{lv} is not obvious for $\theta = 45°, 82°, 133°$, compared to the clear effect for $\theta = 25°$ that an increasing I_v causes a smaller A_{lv} due to the improved cluster connectivity.

3.2.2. Liquid retention curves

The classical liquid retention curves are plotted in Fig. 5 for different disorder indexes and contact angles. The capillary pressure is normalized by the grain diameter d and surface tension γ. It is noted again that the simulation under $I_v = 0.073$ and $\theta = 25°$ is not conducted due to the numerical instability issue. The liquid retention curve has many crucial applications such as characterising the type of soil based on the pore size distribution. Its generic shape is well reproduced by our simulations. It is observed that there is a transition point of saturation at the middle when $\theta < 90°$. Below that saturation, the capillary pressure

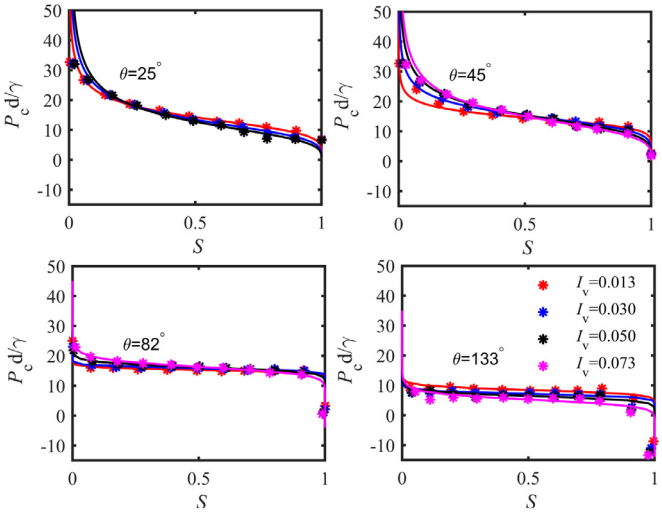

Fig. 5. The liquid retention curves under varied I_v and θ, fitted by van Genuchten equation.

becomes larger with an increasing I_v at a given saturation. Above that saturation, the capillary pressure is smaller with an increasing I_v. The fraction of fine pores is relatively large in a disorder medium. At a low saturation, these fine pores are filled first, enhancing the fluid-solid adhesion and thus enlarging capillary pressure (Li et al., 2018). However, the relatively large pores in a disordered packing remain unoccupied at a higher saturation, which contributes less to the overall capillary pressure. Thus, the capillary pressure decreases with increasing I_v after the middle transition saturation. When the solid surface turns to be hydrophobic, the impact of disorder on liquid retention curves become different shown in Fig. 5 with $\theta = 133°$. The increasing disorder leads to a decreasing capillary pressure at the same saturation. It should be noted that, in order to ensure a nearly zero capillary pressure when the saturation approaches one, a special treatment is applied that the lattice nodes, which are 2 lu away from the grain surface, are excluded in the calculation of the capillary pressure. This is to avoid the transition lattice nodes between the liquid and solid grains.

3.2.3. Cohesive strength

The computed capillary pressure P_c and liquid-solid interfacial area A_{ls} can serve to analyse the cohesive strength of wet granular medium.

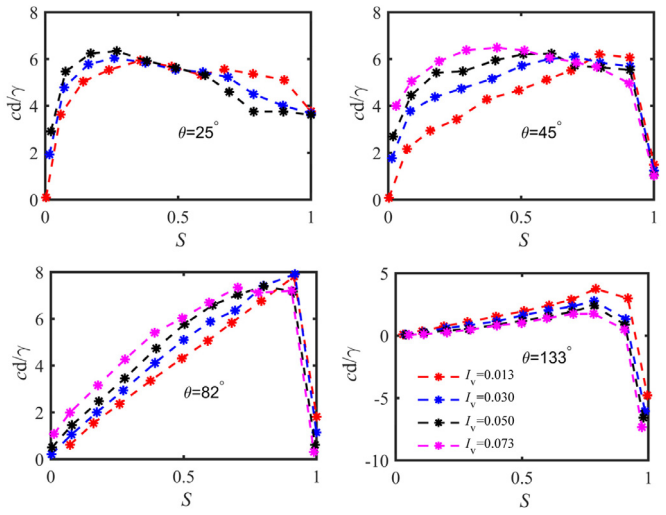

Fig. 6. The normalised cohesive strength as a function of saturation for different disorder at $\theta = 25°, 45°, 82°, 133°$, with dash lines for a guiding purpose.

As the liquid exerts the negative pressure on grains. The average pressure on grains is the sum of normal force divided by the grain surface area. The obtained average pressure is then multiplied by the packing factor ϕ to relate to the scale of packing, as follows (Delenne et al., 2015)

$$c = \frac{A_{ls}}{A_s} P_c \phi. \tag{14}$$

Here, we regard the average grain pressure c as a cohesive strength of the packing induced by the capillary pressure. From Eq. (14), it can be seen that c tends to increase to a maximum value, followed by a drop due to the competition between increasing interfacial area and decreasing capillary pressure, with an increase in liquid saturation. Fig. 6 illustrates cohesive strength curves as a function of saturation when $\theta = 25°, 45°, 82°, 133°$. Similar curves have been generated from other studies (Scheel et al., 2008; Richefeu et al., 2016). It can be seen that the packing with a higher I_v induces a larger cohesive strength and reaches the peak cohesive strength early before a transitional saturation for $\theta = 25°, 45°, 82°$, while an increasing I_v implies a decreasing cohesive strength after the transitional saturation. Besides, the transitional saturation is found to become larger from around 0.5 to 0.8 when θ varies from 25° to 82°. This is due to the disorder effect on the capillary pressure shown from Fig. 5. When $\theta = 133°$, the opposite tendency is found that the cohesive strength decreases with an increasing I_v. Overall, these cohesive strength curves elucidate that the disorder can enhance the cohesive strength in a wet granular medium for $\theta < 90°$ and weaken the cohesive strength for $\theta > 90°$, which contributes to better understanding the mechanical properties of disordered packing and provides a good baseline to design a granular system with the desired cohesive strength.

3.2.4. Soil-water characteristic curves

All of data points in Fig. 5 are further fitted using the famous van Genuchten equation (van Genuchten, 1980) as

$$S(P_c) = S_r + \frac{S_s - S_r}{[1 + (\alpha P_c)^n]^{1-1/n}} \tag{15}$$

where $S_r = 0$ and $S_s = 1$ denotes the residual and saturated liquid saturation, respectively, and α and n are two fitting parameters that relate to the air-entry pressure and pore size distribution, respectively (van Genuchten, 1980). Here, α is inversely proportional to the air-entry pressure which depends on the largest pore in the granular media. A packing with a number of relatively large pores tends to have a small air-entry pressure. As the disorder widens the pore size distribution seen in Fig. 1(c), the packing with a higher I_v tends to have a lower air-entry pressure thus a larger α. Regarding another fitting parameter n, a wet granular packing with a wider pore-size distribution has a steeper liquid retention curve, resulting in a smaller n value, while a packing with a narrow pore-size distribution tends to have a flatter liquid retention curve with a larger n value. It is obvious from Fig. 5 that the disorder is strongly correlated to the slope index n in van Genuchten equation. A larger disorder index represents a wide pore-size distribution shown in Fig. 1(c), which leads to a steeper curve with a smaller slope index n. In the meantime, the wettability can also change the liquid distribution in the wet granular packing. A lower contact angle represents a high affinity of liquid to the solid grain and the liquid can be distributed more easily among pores, therefore resulting in a steeper curve with a lower slope index n as well, shown in Fig. 5. Consequently, both a higher disorder index and a lower contact angle can make a wet granular packing experience a steeper van Genuchten curve.

One important application of van Genuchten equation is to predict the relative permeability. The van Genuchten model is analytically incorporated into the Mualem's relative permeability model shown as (van Genuchten, 1980; Mualem, 1976)

$$K_{rl} = S^{\epsilon}(1 - (1 - S^{1/m})^m)^2 \tag{16}$$

where $m = 1 - 1/n$ is a van Genuchten parameter, related to the symmetry of liquid retention curves, and ϵ is related to the connection between pores and the flow path tortuosity and it can be negative, zero or positive. Although $\epsilon = 0.5$ is widely used in most of studies (Valiantzas, 2011; Mahabadi et al., 2016), the selection of $\epsilon = 0.5$ is originally derived based on fitting experimental data (Mualem, 1976) and there seems to be no clear understanding on ϵ yet. Sheng et al. (2019) adopted $\epsilon = 0$, which also turns out to be feasible.

Additionally, Brooks and Corey (1964) derived the general form for the capillary pressure function as

$$S = (\frac{P_c}{P_b})^{-\lambda}. \tag{17}$$

Here, P_b corresponds to the entry capillary pressure, and λ corresponds to the pore size distribution which is theoretically larger than 0 and becomes smaller for a wider pore size distribution (Brooks and Corey, 1964). As a result, the data points in Fig. 5 are also fitted by using Eq. (17) to compare with the van Genuchten model, shown in next section. This model can also be incorporated into the relative permeability equation as

$$K_{rl} = S^{\frac{2+3\lambda}{\lambda}}. \tag{18}$$

3.2.5. Capillary index

Compared with the parameter related to the entry pressure, we are more interested in slope parameter (i.e., n and λ) as it can be used for the identification of soil type based on the pore-size distribution. As shown in Fig. 5, both a larger I_v and smaller θ can result in the reduction of slope index. To be related with this index, we then propose a capillary index I_c incorporating both disorder and wettability effects given as

$$I_c = \frac{I_v^{\max} - I_v}{I_v^{\max} - I_v^{\min}} \cdot \frac{\cos\theta - \cos\theta_{\min}}{\cos\theta_{\max} - \cos\theta_{\min}}. \tag{19}$$

The form of I_c is developed based on Wang et al.'s 2019 initial proposal. Here, $I_v^{\min} = 0$ representing the disorder index for a regular packing, and $I_v^{\max} = 0.085$ is the maximum disorder index in the current geometry configuration. It changes depending on the geometry packing factor and number of solid grains. The packing with the maximum disorder index allows the contact of solid grains. Moreover, $\theta_{\max} = 90°$ and $\theta_{\min} = 0°$ denote the largest and minimum contact angles, respectively. The maximum contact angle of 90° is selected because the disorder effect on liquid retention curves becomes different when the contact angle is above 90°, and the cases under $\theta = 133°$ are excluded in I_c. Four constant boundary values are considered to formulate the expression of I_c between 0 and 1. The capillary index of 1 stands for the regular packing and the

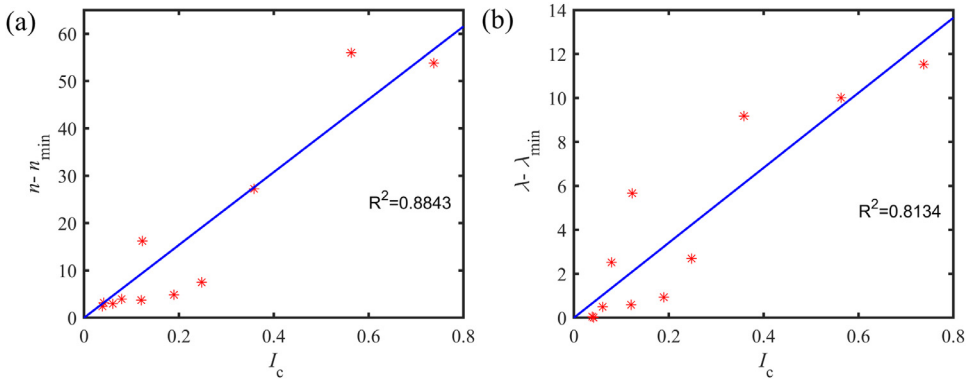

Fig. 7. The slope indexes n and λ as a function of capillary index I_c with proposed linear correlations (blue lines) with R_2 of 0.8843 and 0.8134 for (a) van Genuchten and (b) Brooks-Corey models, respectively.

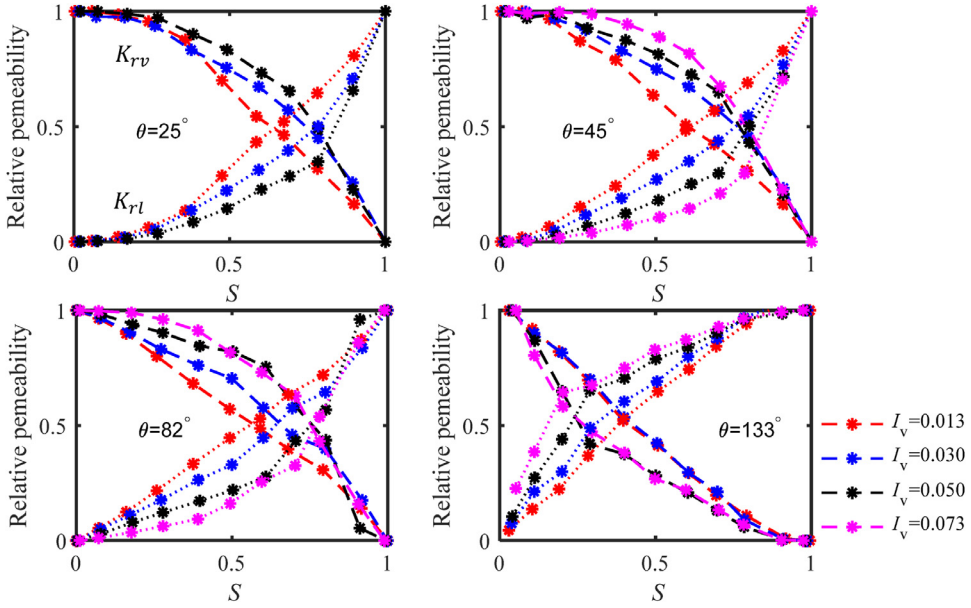

Fig. 8. Relative permeability under different disorder and wettability with dash lines for a guiding purpose.

contact angle of 90°, whilst $I_c = 0$ represents the most disordered packing or the extreme wetting condition. A larger I_c implies a lower I_v and larger θ in Eq. (19), and it corresponds to a larger slope index, which results in a flatter liquid retention curve, while a smaller I_c corresponds to a steeper liquid retention curve. Both slope indexes, n and λ, follow this tendency. Plots of quantitative correlations between I_c and slope indexes are made for both van Genchuten and Brooks-Corey models in Fig. 7, which show strong linear relationships with Pearson correlation coefficients R of 0.9460 and 0.9019, respectively. Based on these high R, a linear relationship between I_c and the slope index is proposed and used to fit the simulation results as

$$g = a \cdot I_c + g_{\min}, \quad g \in \{n, \lambda\} \tag{20}$$

where $g_{\min}$ represents the minimum slope index under the current system, and a denotes the slope of the relationship. This $g_{\min}$ is intrinsically measurable and can be obtained when the input contact angle is set up to be 0 or the most disordered media is applied in the simulation. However, due to the numerical instability reason, the actual $g_{\min}$ is not attained. Consequently, for the slope index n used in the van Genchuten model, $n_{\min} = 1$ is currently selected because n in principle should be larger than 1, and a is then obtained as 76.91 through fitting 11 discrete cases. For the slope index λ in the Brooks-Corey model, a and $\lambda_{\min}$ are obtained as 17.061 and 2.97 through the fitting. Using the proposed correlation between the capillary index and slope index, the capillary pressure-saturation and relative permeability-saturation curve can be obtained for a given granular media with known wettability. In Chen's study (Chen, 2020), a linear fit was conducted between the slope index and dry density. To fit the slope index, Wang et al. (2017) adopted the expression as $n = C_1/\log_{10}C_u + 1$ where C_1 and C_u denote the fitting parameter and the soil gradation parameter, respectively. Here, we provide a first attempt to correlate the slope of water retention curve with properties of liquid and porous media, and such linear correlation has not been reported from available literature. In this study, we focused on the correlation analyses, rather than empirical correlations, thus the linear fitting functions are presented for reference only.

3.2.6. Relative permeability

In addition to the capillary pressure, the relative permeability is another essential parameter to describe the ability of a partially saturated porous medium to transport liquid or air, and it is affected by both topological disorder and wettability. Fig. 8 presents their effects on the relative permeability for both liquid and vapour. The simulation results successfully reproduce the trend of liquid and vapour relative permeability as a function of saturation. For the hydrophilic grain surface, the results show that the liquid relative permeability decreases with an increasing I_v or a decreasing θ at the same saturation. It is because that the high tortuosity in the disorder granular medium and increased liquid-solid adhesion (i.e, larger liquid-solid interfacial area) can intensify the flow resistance, thus leading to the decrease of relative permeability (Li et al., 2018). For the hydrophobic grain surface, the disorder effect shows differently and an increase in I_v can enlarge the liquid relative permeability.

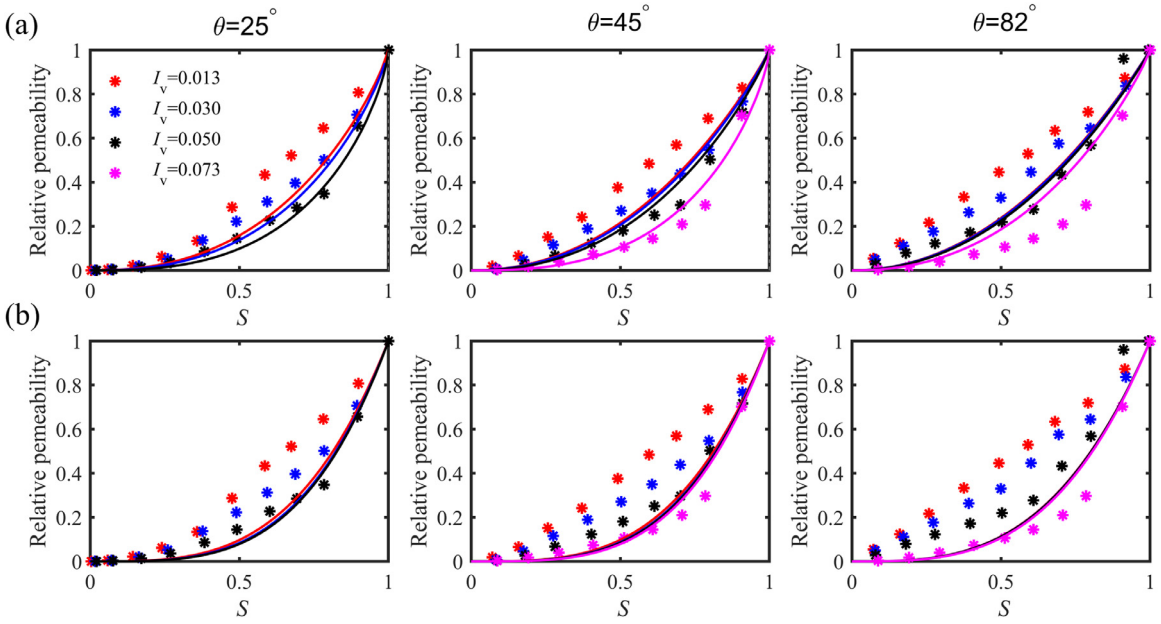

Fig. 9. Comparison between the simulated relative permeability and the solid curves predicted using (a) van Genuchten and (b) Brooks-Corey based relative permeability models at $\theta = 25°, 45°, 82°$.

To predict the relative permeability curve for liquid using Eqs. (16) and (18), the slope indexes, n and λ, are firstly determined from its relation with I_c described in Eq. (20). For the van Genchuten model, n can then be easily converted to $m = 1 - 1/n$ used in the relative permeability equation seen in Eq. (16), and $\epsilon = 0$ is applied (Sheng et al., 2019). The predication of the liquid relative permeability with different wettability is then made in Fig. 9 using both van Genchuten and Brook-Corey models. It is observed that the predication can only provide a qualitative agreement with the experimental simulation results. However, the predication for a higher I_v is in a relatively better consistence with the simulation results as the used two models are derived based on realistic disordered structures. That is, Eqs. (16) and (18) seem not applicable in nearly regular packing. Overall, the van Genchuten-based relatively permeability model is found to be more competent by introducing ϵ to represents the tortuosity and its connection with the pore space. Although a constant ϵ in Eq. (16) is usually employed in most of research (Mualem, 1976; Mahabadi et al., 2016; Valiantzas, 2011; Sheng et al., 2019), we propose that ϵ is not a constant, since freeing ϵ as a fitting parameter can apparently obtain a better consistence. As a result, ϵ should be determined based on the specific granular medium system, and the comprehensive understanding of it and its dependence need further parametric studies by experiments and modelling.

4. Conclusion

In this study, we provide a systematic study on the combined effects of topological disorder and wettability on liquid distribution, interfacial area, capillary pressure and relative permeability under different saturation using the Shan-Chen lattice Boltzmann method. The results show that the connectivity of liquid clusters is enhanced with increasing disorder, leading to earlier transition towards funicular state from pendular state. We also found that the packing structure of grains has profound influence on the interfacial area and capillary pressure across a wide range of saturation. Interestingly, the total liquid-solid interfacial area increases with topological disorder at a wetting condition, while being suppressed when $\theta > 90°$. Consequently, the cohesive strength c, computed as the product of interfacial area and capillary pressure, has similar behaviour.

Further, to unify the impact from disorder and wettability, a capillary index is proposed for estimation of the van Genuchten slope index n and Brooks-Corey slope index λ, providing an effective method for determination of the liquid retention curve and relative permeability curve. It is worth noting that the selection of ϵ in the van Genchuten-based relative permeability equation is based on empirical values. The understanding for it has not reached an agreement, which should be studied in future work.

The evidence from this work highlights the significant impact of topological disorder on liquid distribution and transport phenomena in porous media. Such findings will help expand our understanding of the behavior of unsaturated granular media, especially water retention curve-dependent phenomena. This work also provides a tool for simulating the bubble motion and two-phase flow velocity distribution in the granular system. It would be more interesting to see the bubble coalescence, breakup and trapping, and corresponding velocity profiles in the disordered condition.

Declaration of Competing Interest

The authors declare that they have no known competing financial interests or personal relationships that could have appeared to influence the work reported in this paper.

All the simulations are carried out using the OpenLB open source library (https://www.openlb.net/).

CRediT authorship contribution statement

Zhang Shi: Conceptualization, Methodology, Investigation, Formal analysis, Visualization, Writing - original draft. **Zhongzheng Wang:** Methodology, Investigation, Formal analysis, Writing - review & editing. **Yixiang Gan:** Supervision, Conceptualization, Methodology, Investigation, Writing - review & editing.

Acknowledgments

We are grateful for the financial support from the University of Sydney SOAR Fellowship.

Appendix. Simulations of single-phase flow into disordered porous media

The lattice Boltzmann simulations of single-phase flow based on Eqs. (2) to (5) are conducted to measure the intrinsic permeability of studied porous media. In single-phase flow, there is no need to consider the interparticle and adhesion forces. Only the external force (i.e., gravity in this study) is applied. In the LBM simulations, four disordered media of packing factor of 0.556 with $I_v = 0.013, 0.030, 0.050, 0.073$ are used and the same lattice discretisation as shown in the Method section is followed. Periodic boundary conditions are applied in all directions. The magnitude of kinematic viscosity ν is set to be 0.1667. The magnitude of applied gravity g is 3.2×10^{-4}, and 3×10^4 time steps are completed, which is sufficient to reach the steady state where the intrinsic permeability keeps nearly fixed and is computed as

$$k_i = \frac{q\nu}{g}. \tag{21}$$

Here, q denotes the volume-averaging flux that can be calculated by Eq. (12). Fig. 10 below demonstrates the normalised intrinsic permeability under varied disordered media.

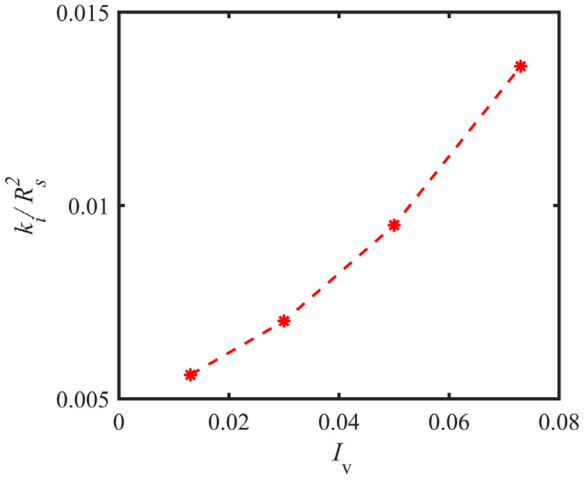

Fig. 10. The normalised intrinsic permeability $k_i/{R_s}^2$ at different I_v.

References

Ahrenholz, B., Tölke, J., Lehmann, P., Peters, A., Kaestner, A., Krafczyk, M., Durner, W., 2008. Prediction of capillary hysteresis in a porous material using lattice-Boltzmann methods and comparison to experimental data and a morphological pore network model. Adv. Water Resour. 31 (9), 1151–1173. https://doi.org/10.1016/j.advwatres.2008.03.009.

Bakhshian, S., Hosseini, S.A., 2019. Pore-scale analysis of supercritical CO2-brine immiscible displacement under fractional-wettability conditions. Adv. Water Resour. 126, 96–107. https://doi.org/10.1016/j.advwatres.2019.02.008.

Bakhshian, S., Hosseini, S.A., Shokri, N., 2019. Pore-scale characteristics of multiphase flow in heterogeneous porous media using the lattice Boltzmann method. Sci. Rep. 9 (1), 3377. https://doi.org/10.1038/s41598-019-39741-x.

Bakhshian, S., Rabbani, H.S., Hosseini, S.A., Shokri, N., 2020. New insights into complex interactions between heterogeneity and wettability influencing two-phase flow in porous media. Geophysical Research Letters 47 (14). https://doi.org/10.1029/2020GL088187. e2020GL088187

Benzi, R., Biferale, L., Sbragaglia, M., Succi, S., Toschi, F., 2006. Mesoscopic modeling of a two-phase flow in the presence of boundaries: the contact angle. Phys. Rev. E 74, 021509. https://doi.org/10.1103/PhysRevE.74.021509.

Bhatnagar, P.L., Gross, E.P., Krook, M., 1954. A model for collision processes in gases. I. Small amplitude processes in charged and neutral one-component systems. Phys. Rev. 94, 511–525. https://doi.org/10.1103/PhysRev.94.511.

Brooks, R.H., Corey, A.T., 1964. Hydraulic Properties of Porous Media. Fort Collins, Colorado: Colorado State University.

Chen, L., Kang, Q., Mu, Y., He, Y.-L., Tao, W.-Q., 2014. A critical review of the pseudopotential multiphase lattice Boltzmann model: methods and applications. Int. J. Heat Mass Transf. 76, 210–236. https://doi.org/10.1016/j.ijheatmasstransfer.2014.04.032.

Chen, Y., 2020. Soil-water retention curves derived as a function of soil dry density. GeoHazards 1 (1), 3–19. https://doi.org/10.3390/geohazards1010002.

Connington, K., Lee, T., 2012. A review of spurious currents in the lattice Boltzmann method for multiphase flows. J. Mech. Sci. Technol. 26 (12), 3857–3863. https://doi.org/10.1007/s12206-012-1011-5.

Cui, G., Liu, M., Dai, W., Gan, Y., 2019. Pore-scale modelling of gravity-driven drainage in disordered porous media. Int. J. Multiphase Flow 114, 19–27. https://doi.org/10.1016/j.ijmultiphaseflow.2019.02.001.

Culligan, K.A., Wildenschild, D., Christensen, B.S.B., Gray, W.G., Rivers, M.L., Tompson, A.F.B., 2004. Interfacial area measurements for unsaturated flow through a porous medium. Water Resources Research 40 (12). https://doi.org/10.1029/2004WR003278. https://agupubs.onlinelibrary.wiley.com/doi/pdf/10.1029/2004WR003278

Delenne, J.-Y., Richefeu, V., Radjai, F., 2015. Liquid clustering and capillary pressure in granular media. J. Fluid Mech. 762, R5. https://doi.org/10.1017/jfm.2014.676.

Ferraro, A., Sufian, A., Russell, A.R., 2017. Analytical derivation of water retention for random monodisperse granular media. Acta Geotechnica 12 (6), 1319–1328. https://doi.org/10.1007/s11440-017-0546-0.

Fournier, Z., Geromichalos, D., Herminghaus, S., Kohonen, M.M., Mugele, F., Scheel, M., Schulz, M., Schulz, B., Schier, C., Seemann, R., Skudelny, A., 2005. Mechanical properties of wet granular materials. J. Phys. 17 (9), S477–S502. https://doi.org/10.1088/0953-8984/17/9/013.

van Genuchten, M.T., 1980. A closed-form equation for predicting the hydraulic conductivity of unsaturated soils. Soil Science Society of America Journal 44 (5), 892–898. https://doi.org/10.2136/sssaj1980.03615995004400050002x. https://acsess.onlinelibrary.wiley.com/doi/pdf/10.2136/sssaj1980.03615995004400050002x

Holtzman, R., 2016. Effects of pore-scale disorder on fluid displacement in partially-wettable porous media. Sci. Rep. 6 (1), 36221. https://doi.org/10.1038/srep36221.

Holtzman, R., Juanes, R., 2010. Crossover from fingering to fracturing in deformable disordered media. Phys. Rev. E 82 (4), 46305. https://doi.org/10.1103/PhysRevE.82.046305.

Hu, R., Lan, T., Wei, G.-J., Chen, Y.-F., 2019. Phase diagram of quasi-static immiscible displacement in disordered porous media. J. Fluid Mech. 875, 448–475. https://doi.org/10.1017/jfm.2019.504.

Huang, H., Lu, X.-y., 2009. Relative permeabilities and coupling effects in steady-state gas-liquid flow in porous media: a lattice Boltzmann study. Phys. Fluids 21 (9), 092104. https://doi.org/10.1063/1.3225144.

Joekar-Niasar, V., Prodanović, M., Wildenschild, D., Hassanizadeh, S.M., 2010. Network model investigation of interfacial area, capillary pressure and saturation relationships in granular porous media. Water Resources Research 46 (6). https://doi.org/10.1029/2009WR008585. https://agupubs.onlinelibrary.wiley.com/doi/pdf/10.1029/2009WR008585

Laubie, H., Monfared, S., Radjaï, F., Pellenq, R., Ulm, F.-J., 2017. Disorder-induced stiffness degradation of highly disordered porous materials. J. Mech. Phys. Solids 106, 207–228. https://doi.org/10.1016/j.jmps.2017.05.008.

Li, Z., Galindo-Torres, S., Yan, G., Scheuermann, A., Li, L., 2018. A lattice Boltzmann investigation of steady-state fluid distribution, capillary pressure and relative permeability of a porous medium: effects of fluid and geometrical properties. Adv. Water Resour. 116, 153–166. https://doi.org/10.1016/j.advwatres.2018.04.009.

Likos, W.J., Jaafar, R., 2013. Pore-scale model for water retention and fluid partitioning of partially saturated granular soil. Journal of Geotechnical and GeoenvironmentalEngineering 139 (5), 724–737. https://doi.org/10.1061/(ASCE)GT.1943-5606.0000811. https://ascelibrary.org/doi/pdf/10.1061/28ASCE29GT.1943-5606.0000811

Likos, W.J., Lu, N., Godt, J.W., 2014. Hysteresis and uncertainty in soil water-retention curve parameters. Journal of Geotechnical andGeoenvironmental Engineering 140 (4), 04013050. https://doi.org/10.1061/(ASCE)GT.1943-5606.0001071. https://ascelibrary.org/doi/pdf/10.1061/28ASCE29GT.1943-5606.0001071

Lu, N.B., Browne, C.A., Amchin, D.B., Nunes, J.K., Datta, S.S., 2019. Controlling capillary fingering using pore size gradients in disordered media. Phys. Rev. Fluids 4, 084303. https://doi.org/10.1103/PhysRevFluids.4.084303.

Mahabadi, N., Dai, S., Seol, Y., Sup Yun, T., Jang, J., 2016. The water retention curve and relative permeability for gas production from hydrate-bearing sediments: pore-network model simulation. Geochemistry, Geophysics, Geosystems 17 (8), 3099–3110. https://doi.org/10.1002/2016GC006372. https://agupubs.onlinelibrary.wiley.com/doi/pdf/10.1002/2016GC006372

Mualem, Y., 1976. A new model for predicting the hydraulic conductivity of unsaturated porous media. Water Resources Research 12 (3), 513–522. https://doi.org/10.1029/WR012i003p00513. https://agupubs.onlinelibrary.wiley.com/doi/pdf/10.1029/WR012i003p00513

Nekoeian, S., Goharrizi, A.S., Jamialahmadi, M., Jafari, S., Sotoudeh, F., 2018. A novel shan and Chen type lattice Boltzmann two phase method to study the capillary pressure curves of an oil water pair in a porous media. Petroleum 4 (3), 347–357. https://doi.org/10.1016/j.petlm.2018.03.010.

Pan, C., Hilpert, M., Miller, C.T., 2004. Lattice-Boltzmann simulation of two-phase flow in porous media. Water Resources Research 40 (1). https://doi.org/10.1029/2003WR002120. https://agupubs.onlinelibrary.wiley.com/doi/pdf/10.1029/2003WR002120

Pan, C., Luo, L.-S., Miller, C.T., 2006. An evaluation of lattice Boltzmann schemes for porous medium flow simulation. Computers & Fluids 35 (8), 898–909. https://doi.org/10.1016/j.compfluid.2005.03.008. Proceedings of the First International Conference for Mesoscopic Methods in Engineering and Science

Porter, M.L., Wildenschild, D., Grant, G., Gerhard, J.I., 2010. Measurement and prediction of the relationship between capillary pressure, saturation, and interfacial area in a NAPL-water-glass bead system. Water Resources Research 46 (8). https://doi.org/10.1029/2009WR007786. https://agupubs.onlinelibrary.wiley.com/doi/pdf/10.1029/2009WR007786

Richefeu, V., Radjai, F., Delenne, J.-Y., 2016. Lattice Boltzmann modelling of liquid distribution in unsaturated granular media. Comput. Geotech. 80, 353–359. https://doi.org/10.1016/j.compgeo.2016.02.017.

Schaap, M.G., Porter, M.L., Christensen, B.S.B., Wildenschild, D., 2007. Comparison of pressure-saturation characteristics derived from computed tomography and lattice Boltzmann simulations. Water Resources Research 43 (12). https://doi.org/10.1029/2006WR005730. https://agupubs.onlinelibrary.wiley.com/doi/pdf/10.1029/2006WR005730

Scheel, M., Seemann, R., Brinkmann, M., Michiel, M.D., Sheppard, A., Herminghaus, S., 2008. Liquid distribution and cohesion in wet granular assemblies beyond the capillary bridge regime. J. Phys. 20 (49), 494236. https://doi.org/10.1088/0953-8984/20/49/494236.

Shan, X., Chen, H., 1994. Simulation of nonideal gases and liquid-gas phase transitions by the lattice Boltzmann equation. Phys. Rev. E 49, 2941–2948. https://doi.org/10.1103/PhysRevE.49.2941.

Sheng, D., 2011. Review of fundamental principles in modelling unsaturated soil behaviour. Comput. Geotech. 38 (6), 757–776. https://doi.org/10.1016/j.compgeo.2011.05.002.

Sheng, J., Huang, T., Ye, Z., Hu, B., Liu, Y., Fan, Q., 2019. Evaluation of van Genuchten-Mualem model on the relative permeability for unsaturated flow in aperture-based fractures. J. Hydrol. 576, 315–324. https://doi.org/10.1016/j.jhydrol.2019.06.047.

Sukop, M.C., Or, D., 2004. Lattice Boltzmann method for modeling liquid-vapor interface configurations in porous media. Water Resources Research 40 (1). https://doi.org/10.1029/2003WR002333. https://agupubs.onlinelibrary.wiley.com/doi/pdf/10.1029/2003WR002333

Tranter, T.G., Gostick, J.T., Burns, A.D., Gale, W.F., 2018. Capillary hysteresis in neutrally wettable fibrous media: a pore network study of a fuel cell electrode. Transp. Porous Media 121 (3), 597–620. https://doi.org/10.1007/s11242-017-0973-2.

Valiantzas, J.D., 2011. Combined Brooks-Corey/Burdine and van Genuchten/Mualem closed-form model for improving prediction of unsaturated conductivity. Journal of Irrigationand Drainage Engineering 137 (4), 223–233. https://doi.org/10.1061/(ASCE)IR.1943-4774.0000284. https://ascelibrary.org/doi/pdf/10.1061

Wang, J.-P., Hu, N., François, B., Lambert, P., 2017. Estimating water retention curves and strength properties of unsaturated sandy soils from basic soil gradation parameters. Water Resources Research 53 (7), 6069–6088. https://doi.org/10.1002/2017WR020411. https://agupubs.onlinelibrary.wiley.com/doi/pdf/10.1002/2017WR020411

Wang, Z., Chauhan, K., Pereira, J.-M., Gan, Y., 2019. Disorder characterization of porous media and its effect on fluid displacement. Phys. Rev. Fluids 4, 034305. https://doi.org/10.1103/PhysRevFluids.4.034305.

Yang, J., Boek, E.S., 2013. A comparison study of multi-component lattice Boltzmann models for flow in porous media applications. Comput. Math. Appl. 65 (6), 882–890. https://doi.org/10.1016/j.camwa.2012.11.022.

Yuan, P., Schaefer, L., 2006. Equations of state in a lattice Boltzmann model. Phys. Fluids 18 (4), 042101. https://doi.org/10.1063/1.2187070.

Zakirov, T., Khramchenkov, M., 2020. Prediction of permeability and tortuosity in heterogeneous porous media using a disorder parameter. Chem. Eng. Sci. 227, 115893. https://doi.org/10.1016/j.ces.2020.115893.

Zhou, A., Huang, R., Sheng, D., 2016. Capillary water retention curve and shear strength of unsaturated soils. Can. Geotech. J. 53 (6), 974–987. https://doi.org/10.1139/cgj-2015-0322.

Zhou, A.-N., 2013. A contact angle-dependent hysteresis model for soil-water retention behaviour. Comput. Geotech. 49, 36–42. https://doi.org/10.1016/j.compgeo.2012.10.004.

Zhu, J.-H., Anderson, S.A., 1998. Determination of shear strength of hawaiian residual soil subjected to rainfall-induced landslides. Géotechnique 48 (1), 73–82. https://doi.org/10.1680/geot.1998.48.1.73.